European Rotorcraft Forum

UNSTEADY BOUNDARY–LAYER TRANSITION MEASUREMENTS AND COMPUTATIONS ON A ROTATING BLADE UNDER CYCLIC PITCH CONDITIONS

Armin Weiss* C. Christian Wolf Kurt Kaufmann Johannes N. Braukmann Markus Raffel
Institute of Aerodynamics and Flow Technology, German Aerospace Center, DLR (Germany)

James T. Heineck
NASA Ames Research Center (USA)

Abstract

The presented work tackles the lack of experimental investigations of unsteady laminar–turbulent boundary–layer transition on rotor blades at cyclic pitch actuation, which are important for accurate performance predictions of helicopters in forward flight. Unsteady transition positions were measured on the blade suction side of a four–bladed subscale rotor by means of the non–intrusive Differential Infrared Thermography (DIT). Experiments were conducted at different rotation rates corresponding to Mach and Reynolds numbers at 75 % rotor radius of up to $M_{75} = 0.21$ and $Re_{75} = 3.3 \times 10^5$ and with varying cyclic blade pitch settings. The setup allowed to measure transition across the outer 54 % of the rotor radius. For comparison, transition was also measured using conventional infrared thermography for steady cases with collective pitch settings only. The study is complemented by numerical simulations including boundary–layer transition modelling based on semi–empirical criteria. Promising results reveal a plausible development of measured transition positions over the pitch cycle, a reasonable comparison to experimental results obtained using the already established σc_p method, and noticeable agreement with numerical simulations. The result is the first systematic study of unsteady boundary–layer transition on a rotor suction side by means of DIT including a comparison to numerical computations.

NOMENCLATURE

A_{blades}	Blade planform area, $A_{\text{blades}} = 2cR$
c	Chord length, $c = 0.072\,\text{m}$
c_l	Sectional lift coefficient, $c_l = (\text{lift}/1\,\text{m}) \,/\, \left[\frac{\rho_\infty}{2} \cdot (2\pi r f_{\text{rotor}})^2 \cdot c\right]$
C_T/σ	Blade loading coefficient
f_{rotor}	Rotation frequency of rotor, Hz
f_{mirror}	Rotation frequency of rotating mirror, Hz
F_{thrust}	Thrust force, N
$I_{\text{pos 1\|2}}$	Image gray levels at pos 1 or pos 2, counts
ΔI_{DIT}	DIT signal, counts
k	Turbulent kinetic energy, m^2/s^2
k_{75}	Reduced frequency, $k_{75} = c/(2 \cdot 0.75\,R)$
M_{75}	Mach number based on $2\pi f_{\text{rotor}} 0.75R$
pos 1|2	Azimuth positions at image acquisition
r	Coordinate in radial direction, m
R	Rotor radius, $R = 0.650\,\text{m}$
Re_{75}	Chord Reynolds number based on $2\pi f_{\text{rotor}} 0.75R$
t	Time, s
T_∞	Total temperature in test section, K
t/T	Phase of pitch cycle, $t/T = t f_{\text{rotor}}$
Tu	Turbulence intensity
U_{loc}	Local flow velocity, m/s
x	Coordinate in chordwise direction, m
v_∞	Wind tunnel flow velocity, m/s
β	Angle between rotor axis and axis of rotating mirror, deg
Θ_{75}	Blade pitch angle at $r/R = 0.75$, deg
$\bar{\Theta}_{75}$	Collective pitch angle at $r/R = 0.75$, deg
$\hat{\Theta}$	Amplitude of cyclic pitch setting, deg
ρ_∞	Density, kg/m^3
$\uparrow$	Upstroke, increasing pitch angle
$\downarrow$	Downstroke, decreasing pitch angle
AHD	Boundary–layer transition criterion according to Arnal, Habiballah and Delcourt
CFD	Computational Fluid Dynamics
DIT	Differential Infrared Thermography
DLR	German Aerospace Center
IR	Infrared
NASA	National Aeronautics and Space

*corresponding author, email: armin.weiss@dlr.de

Copyright Statement

The authors confirm that they, and/or their company or organization, hold copyrights on all of the original material included in this paper. The authors also confirm that they have obtained permission from the copyright holders of any third party material included in this paper to publish it as part of their paper. The authors confirm that they give permission, or have obtained permission from other copyright holders of this paper, for publication and distribution of this paper as part of the ERF proceedings or as individual offprints from the proceedings and for inclusion in a freely accessible web-based repository.

This work is licensed under the Creative Commons Attribution International License (CC BY). Copyright © 2019 by author(s).

	Administration
ONERA	The French Aerospace Lab
RTG	Rotor Test facility of the DLR in Göttingen
RBT	Rotor Blade Transition
TAU	Unstructured finite-volume CFD code
TS	Tollmien–Schlichting
SLS	Strained–Layer Supperlattice

1. INTRODUCTION

Laminar–turbulent boundary–layer transition strongly affects the power requirement of helicopter rotors. Numerical simulations of rotor aerodynamics often do not consider boundary–layer transition. This is due to a lack of appropriate transition models, which must account for the complex three–dimensional and unsteady flow conditions of a rotor in forward flight, and therefore need experimental data for validation.

Measurements of unsteady boundary–layer transition on rotor blades for the validation of transition models are a challenging task. Many experiments reduce the complexity of a rotor setup by investigating boundary–layer transition on periodically pitching airfoils equipped with locally installed fast–response hot–film sensors[1] or dynamic pressure transducers[2]. The application of these techniques in the rotating frame demands the laborious effort of integrating the sensor into the model, yields results at only discrete locations, and possibly disturbs the boundary–layer flow. The techniques have been demonstrated in experiments using hot–film sensors integrated into the blades of a sub–scale helicopter model[3], or pressure transducers in dynamically pitching Mach–scaled rotor blades[4].

Infrared (IR) imaging is well–established to detect boundary–layer transition in steady aerodynamics, such as on rotor blades in hover[5] or climb[6] conditions. Differential Infrared Thermography (DIT) is a non–intrusive optical alternative to locally blade–mounted sensors for the detection of unsteady boundary–layer transition. The basic idea is to subtract two infrared images taken with a short time delay in order to detect the intermediate transition motion. The principle has been demonstrated in proof–of–concept experiments[7], validated against hot-films and dynamic pressure sensors[8], and optimized for various experimental conditions[9].

Recently, Overmeyer et al.[10] applied DIT to the pressure side of a large–scale model rotor in forward flight conditions, showing promising results. Nevertheless, some questions regarding the interpretation of results remain unanswered, most probably due to the influence of the azimuthally varying stagnation temperature of the flow. Gardner et al.[11] investigated boundary–layer transition on the rotor blade suction side of a full–scale EC135 helicopter in forward flight by means of DIT. Due to the challenging experimental setup, e.g. the varying and large distance between the observation helicopter and the test object during formation flight, only a few data points indicating boundary–layer transition have been presented. To the authors knowledge, a systematic experimental study of unsteady boundary–layer transition on a helicopter rotor at cyclic pitch is still missing.

Current approaches to boundary-layer-transition modeling for Computational Fluid Dynamics (CFD) codes face difficult challenges when implemented into rotating systems. Recent activities focused on boundary–layer transition computations of NASA's 'PSP–rotor' experiment in hover[12,13,14,15] and forward flight[16], as well as on the S–76 rotor in hover[17].

Investigations at the German Aerospace Center (DLR) and at the French Aerospace Lab (ONERA) have shown that approximate transition modeling in unsteady Reynolds–averaged Navier-Stokes simulations can provide an improved prediction of the rotor performance in hover[18,19] and forward flight[19,20] when using relatively coarse grids, which are especially applicable to industrial aircraft development efforts. The GOAHEAD data set[3] was used for validation but the available hot-film data is too sparsely sampled to provide reliable validation of the codes.

In the framework of a DLR–ONERA cooperation, boundary–layer–transition computations[21] were performed that have shown promising results when compared to experimental data sets obtained on a two–bladed Mach–scaled rotor under collective[6] and cyclic[4] pitch conditions in the Rotor Test Facility (RTG[22]) at DLR Göttingen. Still, the computations of the cyclic test case showed the need for spatially highly resolved measurements of unsteady boundary–layer transition.

In this paper, unsteady boundary–layer transition is investigated on the four–bladed subscale model rotor of the well–instrumented RTG. The experiments include a variation of cyclic blade pitch angles at different rotation frequencies as well as cases with only collective pitch settings. Two of the main objectives are to evaluate the feasibility of DIT measurements under rotor conditions and to investigate the effect of different pitch rates on unsteady boundary–layer transition positions by independent variation of pitch amplitude and frequency. Measured data are further compared to unsteady boundary–layer transition computations using the DLR-TAU code and the Rotor Blade Transition (RBT) tool as recently applied by Kaufmann et

This work is licensed under the Creative Commons Attribution International License (CC BY). Copyright © 2019 by author(s).

Table 1: Test conditions

Test case	f_{rotor}, Hz	$\bar{\Theta}_{75}$, deg	$\hat{\Theta}$, deg	Re_{75}	M_{75}	v_∞, m/s	k_{75}
i	11.8	10.1	1.6	1.7×10^5	0.11	2.2	
ii	12.0	10.1	2.9	1.7×10^5	0.11	2.2	
iii	11.8	9.9	6.2	1.6×10^5	0.10	2.2	0.074
iv	23.6	9.6	6.2	3.3×10^5	0.21	2.2	
v	23.6	9.0	5.9	3.2×10^5	0.21	4.9	
steady	23.6	$2.1 - 17.1$	-	$3.2 - 3.3 \times 10^5$	0.21	4.9	-

al.[21] The result is the first systematic study of unsteady boundary–layer transition on a rotor suction side by means of DIT including a comparison to numerical prediction capabilities at DLR.

2. EXPERIMENTAL AND NUMERICAL SETUP

2.1. Experimental Setup

The experiments were conducted at RTG[22] of the DLR in Göttingen. The four–bladed rotor (see Fig. 1) was placed into the test section of an Eiffel–type wind tunnel with a nozzle cross section of 1.6 m x 3.4 m. The rotor axis is horizontal and a slow axial inflow ($v_\infty = 2.2; 4.9$ m/s) was provided to prevent recirculation of tip vortices and blade–vortex interaction.

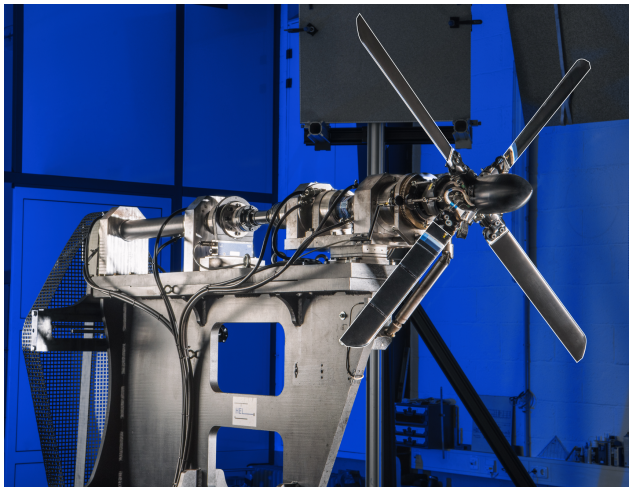


Figure 1: Four–bladed rotor with parabolic blade tips (see Fig. 2) in the RTG at DLR Göttingen

The rotor blades (see Fig.2) were made out of carbon fiber reinforced plastic, had a radius of $R = 0.650$ m, a chord length of $c = 0.072$ m and a relative thickness of 9 %. The blades were equipped with the DSA–9A helicopter airfoil and comprised a parabolic SPP8 tip without anhedral[23], which started at 91 % radius and led to a tip chord length of 0.024 m (see Schwermer et al.[22] for details). A negative linear twist of -9.33 deg was incorporated

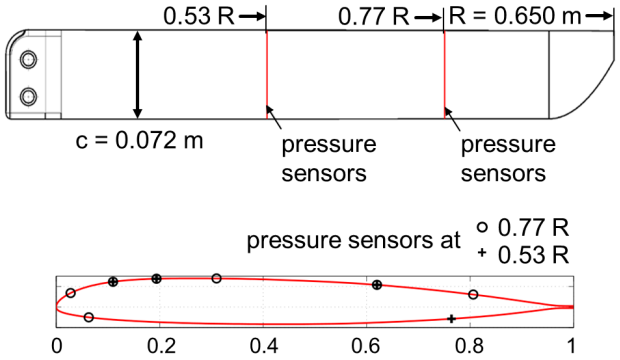


Figure 2: *Top:* Planview of the rotor blade[22] (not to scale) *Bottom:* DSA–9A airfoil and location of pressure sensors

along the blades' span between $0.25 < r/R < 1$. The investigated blade was equipped with fast response pressure transducers at $r/R = 0.53$ and at $r/R = 0.77$ (see Fig. 2, *bottom*), providing a signal at a bandwidth of 19 kHz.

The rotor head of the RTG featured a swashplate allowing for the adjustment of both collective and cyclic blade pitch angles[22]. The resulting pitch cycle at $r/R = 0.75$ can be described according to Eq. 1.

(1) $\quad \Theta_{75} = \bar{\Theta}_{75} - \hat{\Theta} \cdot cos(2\pi f_{\text{rotor}} t)$

In this expression, $\bar{\Theta}_{75}$ and $\hat{\Theta}$ are the collective and cyclic pitch settings, and $f_{\text{rotor}} t = t/T$ is the phase position. With this setting, the pitch cycle started at minimum pitch angle at $t/T = 0$ and reached the maximum at $t/T = 0.5$. While the optical setup was oriented towards a fixed azimuthal blade position, the test rig allowed to scan the entire pitch cycle within the camera's field of view at that azimuthal position[4]. This was realized by slowly rotating the usually stationary lower part of the swashplate, leading to the blade pitch cycle sweeping through the fixed measurement position.

A schematic sketch of the test setup is shown in Fig. 3. Heat lamps were installed above the nozzle outlet in order to increase the temperature difference between laminar and turbulent flow regions on the blade surface. The resulting radiative heat

This work is licensed under the Creative Commons Attribution International License (CC BY). Copyright © 2019 by author(s).

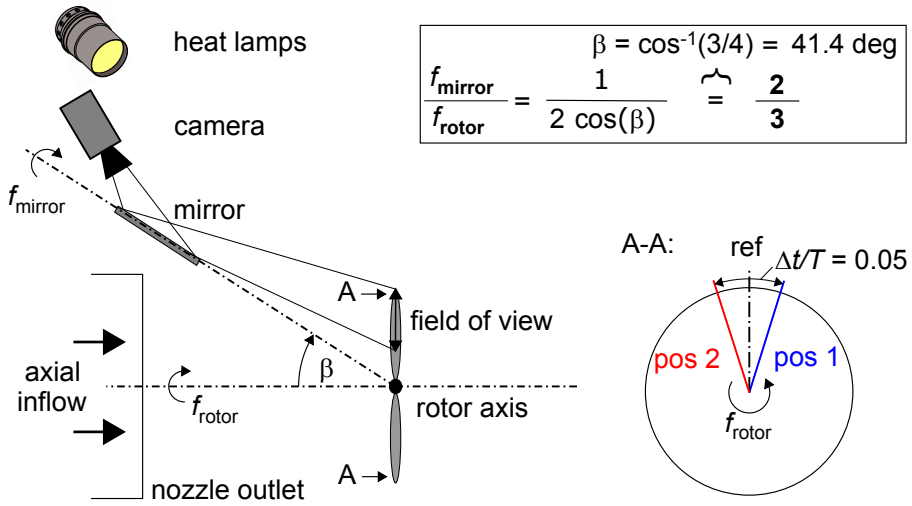


Figure 3: Schematic of rotating mirror setup in off–axis configuration for DIT measurements at the RTG

flux was measured with a power meter and yielded between $400 - 500\,\mathrm{W/m^2}$ at the rotor disk. Images were acquired with a FLIR Systems™ X8500sc SLS high speed infrared camera. The $14\,\mathrm{bit}$ camera had a spectral sensitivity in the long wave infrared range of 7.5 – $12\,\mu\mathrm{m}$ and was equipped with a $50\,\mathrm{mm}$, f/2.5 lens approximately $2\,\mathrm{m}$ apart from the investigated blade. The optical setup was completed by a rotating mirror, which was used to capture a stationary image of the moving blade. This enabled longer exposure times for increased signal strength whilst avoiding motion–blurred images.

An important feature of the rotating mirror is that it allows to capture two successive rotor blade images within the same rotor revolution at different azimuthal positions, which correspond to different pitch phases. The rotating mirror was installed in an off–axis configuration as suggested by Raffel and Heineck[24]. It meets the requirement for a ratio of rotation frequencies between rotating mirror to rotor of $f_{\mathrm{mirror}}/f_{\mathrm{rotor}} = 2/3$. The ratio enables image acquisition at every third rotor revolution. Consequently, the setup aims to acquire an image pair (at 'pos 1' and 'pos 2', see Fig. 3) at all pitch phases and with a phase difference during a single rotor revolution. This allows to capture the instantaneous boundary–layer transition position associated with the pitch angle at the intermediate phase position (marked as 'ref' in Fig. 3).

The examined test cases are listed in Tab. 1. The resulting Mach- and Reynolds numbers as well as the reduced frequency k_{75} are provided at the radius $r = 0.75\,R$. The test cases comprise three different pitch amplitudes and two different rotation rates of the rotor, allowing to study the effects of pitch amplitude (test cases i,ii and iii) and pitch frequency (test cases iii and iv) independently. Test case v was selected for comparison to the steady cases with constant collective pitch angle and to numerical simulations, which are described in the next section.

2.2. Numerical Setup

DLR-TAU[25] is an unstructured finite-volume CFD code solving the compressible Navier-Stokes equations. The temporal discretization of the RBT simulations uses an implicit Euler method with a LUSGS linear solver inside a dual time stepping approach. The turbulence and transition equations are solved by a Roe scheme with a second order state extrapolation, and for the diffusive fluxes a second order central scheme is used. The turbulence is modeled using the k-ω SST eddy viscosity model according to Menter[26].

Both highly-resolved and partially scale-resolving transition computations on the NASA PSP rotor by e.g. Coder[12] and Vieira et al.[13] have shown the potential of a very detailed transition modeling. Nevertheless, the computational costs of these kind of investigations are still too high for industry–relevant computations. In this study, a very coarse grid and an approximate boundary–layer transition method is used, which are interesting for industry–relevant studies due to the low computational costs. The computations were performed using the GCS Supercomputer SuperMUC at the Leibniz Supercomputing Centre. The computations without cyclic lasted $\approx 10\,000\,\mathrm{CPUh}$, whereas the cyclic test case v (see Tab. 1) took $\approx 20\,000\,\mathrm{CPUh}$ to converge .

The RBT-TAU computations were run on a complete four blade mesh setup-up, which is depicted in Fig. 4. The hybrid mesh consists of a hexahedral grid around the blade and tetrahedral elements in

This work is licensed under the Creative Commons Attribution International License (CC BY). Copyright © 2019 by author(s).

the farfield. The background farfield mesh is integrated with the blade mesh using the chimera technique. A full cylinder of $200\ R$ height and $100\ R$ radius containing the four blades is used for the RBT computations. Each blade mesh of the RBT case comprises 1.5×10^6 points resulting in a total mesh size of 7.7×10^6 nodes (see Fig. 4). The first wall spacing was set to keep $y^+ < 1$. The blade is discretized with 120 points and 100 points in streamwise and radial direction, respectively. The boundary-layer discretization in wall–normal direction comprises approximately 30 points.

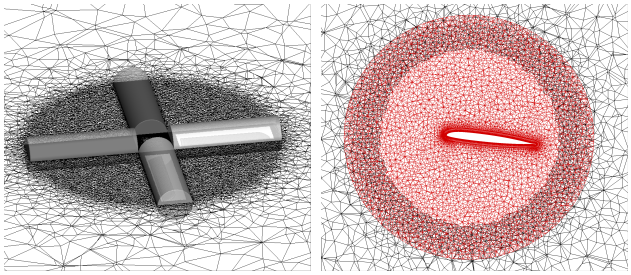


Figure 4: *Left:* Chimera setup for rotor blades; *Right:* Grid sections at $r/R = 0.77$

The RBT tool, which is linked to the DLR-TAU code, will be discussed briefly. For a more detailed description, the reader is referred to Heister et al.[20] Although the RBT tool is capable of detecting five different types of transition mechanisms, only the criterion to predict Tollmien–Schlichting (TS) transition according to Arnal, Habiballah and Delcourt[27] (AHD) is used in this study. Kaufmann et al.[21] have shown in preceding computations of the same rotor in a two–bladed configuration that the prediction, using all types of transition mechanisms, results in an erroneous transition position and that the prediction is only acceptable, if TS transition is used.

To evaluate the AHD criteron, section cuts at 48 different radii are defined for both the pressure and the suction side. The computed transition onset positions are then used to control the turbulence model. However, the transitional region is not modeled, i.e. point transition is assumed. To compute the local turbulence level Tu , using Eq. 2, the flow velocities U_{loc} and the turbulent kinetic energy k are extracted from the numerical data at a user-defined distance upstream of the corresponding stagnation point.

$$Tu = 1/U_{\text{loc}}\sqrt{2/3\,k} \tag{2}$$

To align with the experimental turbulence level, the kinetic energy at the far field boundary has to be set to match the extracted kinetic energy in front of the profile sections. Therefore, the sustaining turbulence concept is locally implemented up to one rotor radius above the rotor in order to reduce the dissipation of the turbulence quantities from the farfield to the rotor[28]. For the DLR-TAU transition criteria computations, an iterative approach was applied to match the turbulence level of $Tu = 0.09\,\%$ at $r/R = 0.77$. The value for Tu was deduced by Weiss et al.[29], who conducted transition measurements on the two–bladed DSA–9A rotor in the same facility.

3. DATA ACQUISITION AND PROCESSING

3.1. Steady Boundary–Layer Transition Measurements

For the steady test cases in Tab. 1, IR images were exposed for 57 µs and acquired as the blade was passing the azimuthal 'ref' position (see Fig. 3). For each data point, chordwise positions were extracted at various radial positions corresponding to boundary–layer transition $(x/c)_{\text{tr}}$ (at 50 % turbulence intermittency), transition onset $(x/c)_{\text{onset}}$, and transition end $(x/c)_{\text{end}}$. Image processing was carried out according to the automated procedure as detailed by Weiss et al.[6] In this work, sixteen images were averaged to increase the signal to noise ratio.

3.2. Unsteady Boundary–Layer Transition Measurements

With every third blade revolution IR images were acquired as the blade was passing the azimuthal positions pos 1 and pos 2 (see Fig. 3) at an exposure time of 150 µs. The azimuthal positions were phase–separated by $\Delta t/T = \Delta t f_{\text{rotor}} = 0.05$ at all test conditions. The resulting separation times of the image pairs within the same revolution were $\Delta t = 4.2$ ms and 2.1 ms at $f_{\text{rotor}} = 11.8$ Hz and 23.6 Hz, respectively. The separation time was limited by the camera's pixel clock and the selected region of interest, which covers 54 % of the rotor radius at a resolution of ≈ 2 px/mm (see Fig. 5). At each test condition, the full pitch cycle was recorded by acquiring ≈ 1000 image pairs at pos 1 and pos 2, respectively. The resulting phase resolution of the DIT signal is $\Delta t/T \approx 0.001$. Since image pairs were acquired with every third blade revolution, data acquisition took approximately 4 min and 2 min for each data point at $f_{\text{rotor}} = 11.8$ Hz and 23.6 Hz, respectively.

The raw image shown in Fig. 5 was acquired for test case ii. The displayed gray levels on the blade surface scale with temperature and appear

This work is licensed under the Creative Commons Attribution International License (CC BY). Copyright © 2019 by author(s).

darker in regions of comparatively high heat transfer, for instance close to the leading edge, where the boundary layer is thin, or in the turbulent wake of the roughness element.

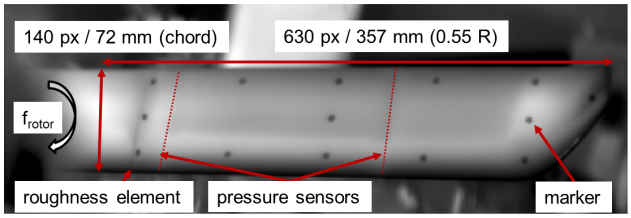


Figure 5: Sample image acquired at f_{rotor} = 12.0 Hz, $\bar{\Theta}_{75} = 10.1\,\mathrm{deg}$ and $\hat{\Theta} = 2.9\,\mathrm{deg}$

Other than for the steady test cases with only collective pitch settings (see Sec. 4.1), the measured intensity gradients in tangential direction cannot be used for instantaneous boundary–layer transition detection on dynamically pitching rotor blades. Previous studies on 2D pitching airfoils have shown that the spatial gradients in the raw images are influenced by the thermal inertia of the model surface[7,9,30]. Hence, the DIT approach aims to subtract two infrared images acquired at a short time or phase difference within the pitch cycle to capture the transition motion between the two instants at different pitch angles. With this approach, the time–averaged temperature footprint on the model surface is canceled out. In previous DIT studies, the two images were acquired in different pitch cycles at a defined phase difference because of the limited temporal resolution of the infrared camera, see e.g. Raffel et al.[7] Wolf et al.[9] showed that the resulting large time difference between images can cause global temperature drifts on the model surface, which need to be corrected. In this study, however, the applied infrared camera allowed to capture images during the same rotor revolution at time differences corresponding to acquisition frequencies of up to 476 Hz at the resolution and field of view as described above.

In order to subtract gray levels at the same physical position on the blade, image alignment is necessary. Therefore, round markers (see Fig. 5 and Fig. 6) were applied onto the blade surface. Similar as for the steady test cases, marker registration and image alignment were performed with the in–house developed software package *ToPas* (as in Klein et al.[31]). The procedure accounts for rotation and translation within the image plane. Noise was removed by applying a 3×5 moving average filter in chordwise and spanwise directions. The aligned images were sorted by phase and the DIT signal ΔI_{DIT} was obtained for each phase according to Eq. 3.

$$\Delta I_{\mathrm{DIT}}\left(t/T\right) = \left[I\left(t/T\right)_{\mathrm{pos1}} - \bar{I}_{\mathrm{pos1}}\right] - \left[I\left(t/T\right)_{\mathrm{pos2}} - \bar{I}_{\mathrm{pos2}}\right] \tag{3}$$

Before subtraction of the images at pos 1 and pos 2, tare images according to Eq. 4 are subtracted.

$$\bar{I}_{\mathrm{pos1|2}} = \frac{1}{N}\sum_{i=1}^{N(\approx 1000)}\left[I\left(t/T\right)_{\mathrm{pos1|2}}\right]_i \tag{4}$$

Subtraction of these images accounts for any systematic differences between the two azimuthal positions, for instance due to inhomogeneous heating of the rotor disc area. The phase t/T, which is associated with the result, corresponds to the mean value of the processed images and the azimuthal position marked as 'ref' in Fig. 3, i.e. $t/T = \left[\left(t/T\right)_{\mathrm{pos1}} + \left(t/T\right)_{\mathrm{pos2}}\right]/2$. The resulting DIT signal has been dewarped to blade coordinates in Matlab applying a projective image transformation function to calibrated marker coordinates, which have automatically been detected.

4. RESULTS

4.1. Steady Boundary–Layer Transition

A sample result of the steady transition measurement is displayed in Fig. 6. The positions corresponding to boundary–layer transition $(x/c)_{\mathrm{tr}}$, transition onset $(x/c)_{\mathrm{onset}}$, and transition end $(x/c)_{\mathrm{end}}$ are plotted as red lines over the corresponding dewarped IR image. The bright and dark regimes in the image correspond to less and more efficient cooling of the heated blade surface. As argued by Weiss et al.[6], the points denoted as $(x/c)_{\mathrm{tr}}$ are extracted at the largest intensity gradient of the IR signal from bright to dark and therefore correspond to the point of 50 % turbulence intermittency[32,33,34]. The points denoted as $(x/c)_{\mathrm{onset}}$ and $(x/c)_{\mathrm{end}}$ are

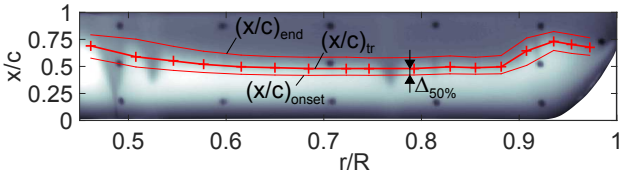


Figure 6: Measured transition positions, transition onset and end (in red) over corresponding infrared image at $\Theta_{75} = 10.0\,\mathrm{deg}$, f_{rotor} = 23.6 Hz and v_∞ = 4.9 m/s, rotation is clockwise

This work is licensed under the Creative Commons Attribution International License (CC BY). Copyright © 2019 by author(s).

detected in the vicinity of the local maximum curvature of the IR signal upstream and downstream of $(x/c)_{\mathrm{tr}}$ and therefore correspond to the onset and end of the transition region[32,33]. The visible turbulent wedges are caused by a roughness element, which was applied at $r/R = 0.49$ as well as triggered by the pressure tap cavities at $r/R = 0.53$ and $r/R = 0.77$ (see Fig. 5).

The thrust is evaluated in terms of the blade loading coefficient $C_T/\sigma = F_{\mathrm{thrust}} / \left[\rho_\infty A_{\mathrm{blades}} (2\pi f_{\mathrm{rotor}} R)^2\right]$. Experimental and numerical results for the steady test cases are plotted against the pitch angle in Fig. 7. The bar sizes indicate the linearity error of the piezo-balance being $\pm$ 1 % of the measured value but at least $\pm$ 1 N. The numerical results exceed the experimental data at lower pitch angles by up to $\Delta C_T/\sigma = 0.004$ while agreeing within the accuracy limits of the experimental results at the highest pitch angles tested.

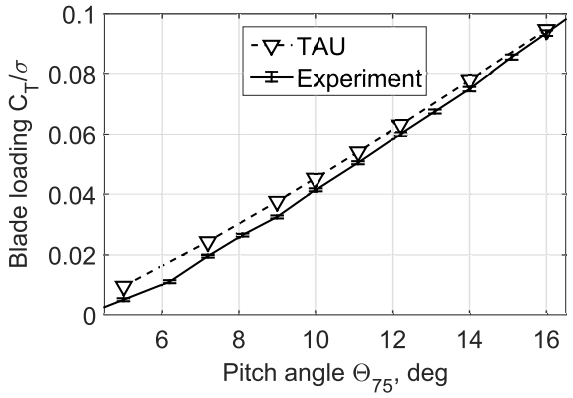


Figure 7: Comparison between measured and simulated blade loading for steady test cases at f_{rotor} = 23.6 Hz and v_∞ = 4.9 m/s

For the numerical boundary–layer transition solution, the AHD criterion estimates the point of primary instability of TS waves. Therefore, the simulated results represent the transition onset. In order to compare experimental and numerical transition positions corresponding to 50 % intermittency (as detected by DIT for the unsteady cases, see Sec. 4.2), the numerical results for $(x/c)_{\mathrm{onset}}$ have to be corrected. The measured difference between the experimental transition position and transition onset, $\Delta_{50\,\%} = (x/c)_{\mathrm{tr}} - (x/c)_{\mathrm{onset}}$, is plotted as function of $(x/c)_{\mathrm{onset}}$ for all steady test cases at various radial positions (see red '+'-signs in Fig. 6) in Fig. 8. The fitted and dashed curve in red is further used as a correction function. The corresponding values of $\Delta_{50\,\%}$ are added to the numerical transition onset to enable comparability to experimental transition positions. The correction function can be interpreted as an intermittency function describing approximately half of the intermittency length along the streamwise coordinate where transition onset is detected. The values reveal a dependency on the streamwise coordinate with a peak at $(x/c)_{\mathrm{onset}} = 0.6$. It is known that the intermittency length increases as the adverse pressure gradient becomes weaker[35]. Previous investigations[29] of static transition data on the same rotor blade have shown that the boundary–layer shape factor at transition onset exhibits its minimum in the vicinity of $x/c = 0.6$. The lowest shape factor corresponds to the weakest adverse pressure gradient[36], which therefore explains the distribution of $\Delta_{50\,\%}$ in Fig. 8. Richter et al.[37] measured the full intermittency region on a 2D pitching DSA–9A airfoil suction side with hot–films at $M = 0.3$ and $Re = 1.8 \times 10^6$. Their results are added to Fig. 8. In order to compare only half of the intermittency lengths, their values are divided by two, which yields good agreement with the results from this study. Their unsteady results at pitch angles between 4 deg $\pm$ 6 deg and a reduced frequency of 0.060 revealed insignificant differences to the steady data, which justifies the applicability of the correction function to unsteady cases.

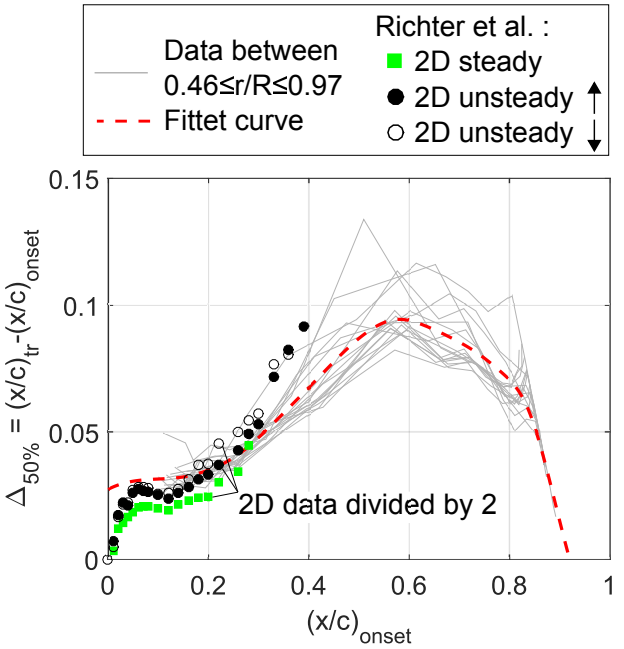


Figure 8: Intermittency correction function against transition onset and comparison to 2D airfoil data from Richter et al.[37]

Measured and calculated transition results for steady test cases at $\Theta_{75} = 9\,\mathrm{deg}$ and $14\,\mathrm{deg}$ are plotted against the radial coordinate in Fig. 9 (*top*), while the corresponding numerical sectional lift coefficients c_l are depicted in Fig. 9 (*bottom*).

The larger lift and the resulting stronger adverse

This work is licensed under the Creative Commons Attribution International License (CC BY). Copyright © 2019 by author(s).

pressure gradients on the blade suction side lead to further upstream transition positions at $\Theta_{75} = 14\,\mathrm{deg}$. At this pitch angle, measured and calculated values for both $(x/c)_{\mathrm{tr}}$ and $(x/c)_{\mathrm{onset}}$ coincide. For both cases, the experimentally deduced downstream kink of transition positions at $r/R > 0.9$ is appropriately predicted by the numerical results. The effect can be attributed to the influence of the blade tip vortex, which is also reflected in the spanwise development of the sectional lift coefficient in the graph below. The lift curves comprise a minimum at $r/R = 0.93$ which is in the spanwise range with the downstream kink of transition positions. At $\Theta_{75} = 9\,\mathrm{deg}$ measured and numerically corrected results for $(x/c)_{\mathrm{tr}}$ show close agreement at $r/R < 0.72$ and at $r/R > 0.9$, which demonstrates that the correction function $\Delta_{50\,\%}$ works well. In the spanwise range between $0.72 < r/R < 0.9$ the numerical results switch between two levels and deviate by up to $\Delta\ (x/c)_{\mathrm{tr}} \approx 0.21$ further upstream. It is known from previous steady transition investigations on the same rotor blade[29] that the transition gradient with changing pitch angles is comparatively large in this streamwise range. Hence, the case at $\Theta_{75} = 9\,\mathrm{deg}$ exemplifies that transition positions in this streamwise range are challenging to predict, which was also observed by Kaufmann et al.[21] for steady cases with the two–bladed rotor configuration at the RTG.

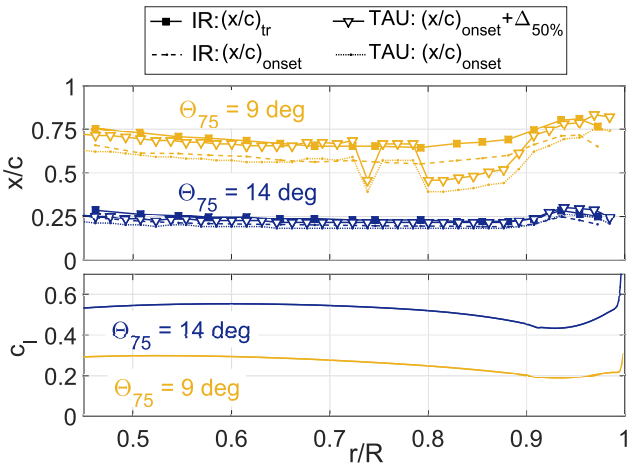


Figure 9: Measured (IR) and calculated (TAU) transition data across the blade span (*top*) and calculated sectional lift coefficients (*bottom*) for selected steady test cases

4.2. Unsteady Boundary–Layer Transition

Selected DIT results obtained at test case v (see Tab. 1) during upstroke (↑) and downstroke (↓) are shown in Fig. 10 *(top)* and Fig. 10 *(bottom)*. The results were obtained at the same instantaneous pitch angle of $\Theta_{75} = 11.5\,\mathrm{deg}$. During upstroke, boundary–layer transition moves upstream between the first and the second image. Hence, the spatial extent of more efficiently cooled blade surface is increased and the DIT signal is expected to be positive. The opposite holds true during downstroke. This is confirmed by the results in Fig. 10. At $t/T = 0.317$, the DIT signal is positive and appears as yellow band across the blade span. In contrast, the result at $t/T = 0.683$ on the bottom reveals a prominent band of negative values for ΔI_{DIT} at $r/R > 0.55$, which are caused by the downstream movement of boundary–layer transition during downstroke. In Fig. 10 *(top)*, wedge–shaped structures can be distinguished in the DIT signal at $r/R = 0.49, 0.53$ and 0.77. They correspond to turbulent wedges caused by the roughness element and the pressure tap cavities as was the case for the steady results in Fig. 6.

The transition position is quantified at $r/R = 0.8$ by analysis of the spanwise averaged signal confined by the red lines in Fig. 10 (*top*) and Fig. 10 (*bottom*). The averaging interval corresponds to $\Delta r = 10\,\mathrm{mm}$ and the corresponding DIT signals are plotted versus the streamwise coordinate x/c in Fig. 10 (*right*). The processed DIT data, displayed by the solid and dashed lines for $t/T = 0.317$ and $t/T = 0.683$, were used to find the circled signal peaks. According to Richter et al.[8] and Gardner et al.[30], the DIT peak locations are equivalent to the positions corresponding to $50\,\%$ turbulence intermittency. The DIT peak location is also at the position where the cycle–to–cycle RMS pressure transducer signal peaks (according to the so–called σc_p method[2]), and therefore considered as the transition position $(x/c)_{\mathrm{tr}}$ in this work. A comparison of the peak positions in Fig. 10 (*right*) reveals that transition occurs further upstream by $\Delta(x/c)_{\mathrm{tr}} \approx 0.4$ at $t/T = 0.683$ during downstroke compared to $t/T = 0.317$ during upstroke. Considering that the associated pitch angle is the same for both phases, the observed difference is due to both aerodynamic and temperature–lag related hysteresis effects as previously examined by Gardner et al.[30] and Wolf et al.[9] and further discussed below.

For test case v, the DIT signal ΔI_{DIT} was analyzed at $r/R = 0.8$ for all sampled pitch phases. An automated algorithm detected the peak height ΔI_{DIT} and the corresponding transition position $(x/c)_{\mathrm{tr}}$, which are plotted in Fig. 11 (*top*) and (*bottom*), respectively. The peak search region was confined to ± 0.4 chord lengths around the steady transition position at the same pitch angle. The steady case data were linearly interpolated between the measured points, which are displayed by squares in Fig. 11 (*bottom*). The selected search region includes hys-

This work is licensed under the Creative Commons Attribution International License (CC BY). Copyright © 2019 by author(s).

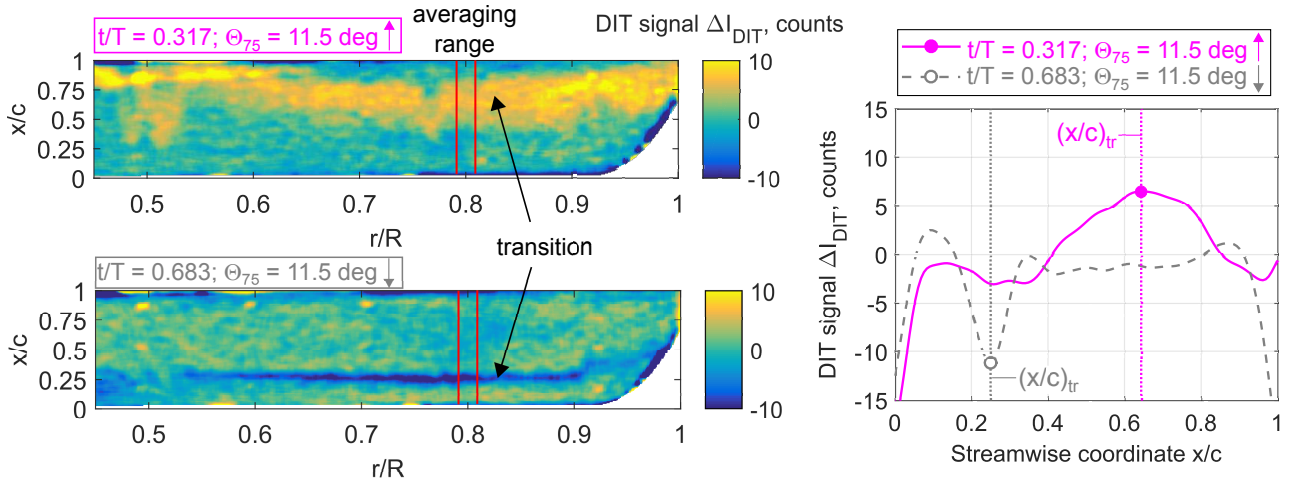


Figure 10: DIT results for test case v (see Tab. 1) at an instantaneous pitch angle of $\Theta_{75} = 11.5\,\mathrm{deg} \uparrow$ (*top*) and $\downarrow$ (*bottom*) with spanwise averaged DIT signals at $r/R = 0.8$ against streamwise coordinate (*right*)

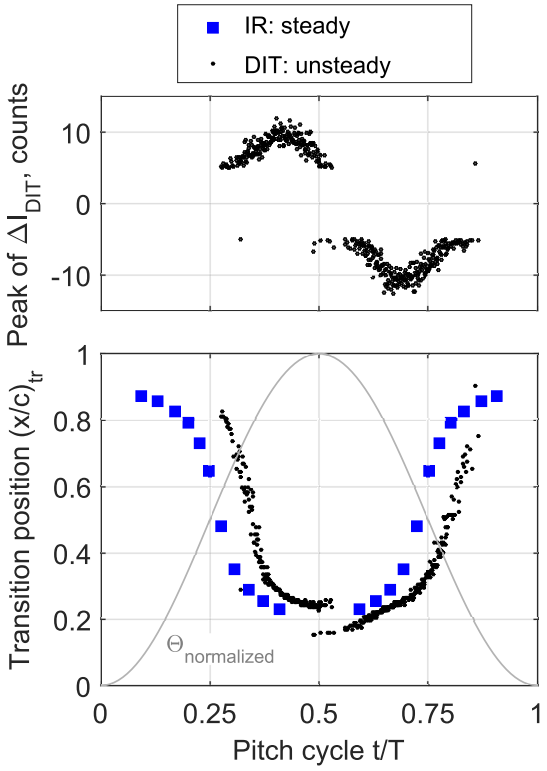


Figure 11: DIT results for test case v at $r/R = 0.8$: Signal peaks against pitch cycle (*top*); measured unsteady transition positions against pitch cycle compared to transition positions of steady cases (see Tab. 1) at associated pitch angles (*bottom*)

teresis effects and removes invalid outliers. For all other test cases, the search region was confined to ± 0.25 chord lengths around the transition position detected at the previous phase sample. Peaks were only accepted above a threshold value of $|\Delta I_{\mathrm{DIT}}| > 5\,\mathrm{counts}$. The qualitative evolution of the pitch angle is added in gray to Fig. 11 (*bottom*) to ease interpretation of the results. Transition detection is difficult at the reverse points of the pitch cycle because DIT relies on changes of the boundary–layer transition position. Similar to the findings in previous DIT studies[7,8,9], the data gap at the downstream transition reverse point close to the pitch minimum is larger than the phase range with spurious data at the pitch maximum reverse point. At the upstream reversal of $(x/c)_{\mathrm{tr}}$, the detected peak positions switch back and forth between distinct chordwise positions. Richter et al.[8] and Wolf et al.[9] found that this behavior is due to the coexistence of the positive and negative signal peaks, which are associated with the upstream and downstream movement of transition (see Fig. 11, *bottom*).

As expected, transition moves upstream at increasing pitch angles and downstream at decreasing pitch angles. The DIT peaks in Fig. 11 (*top*) are large when the transition motion between the images at pos 1 and pos 2 is fast. Therefore, the peak values have a sinusoidally–shaped distribution over the pitch cycle t/T as also previously observed by Wolf et al.[9] The measured unsteady transition positions in Fig. 11 (*bottom*) are spread across a similar chordwise range as compared to the steady IR results, yet exhibit a phase lag of $\Delta t/T \approx 0.1$. The underlying hysteresis effects are further discussed below.

4.2.1. Pitch Rate Effects on Unsteady Boundary–Layer Transition

The effect of pitch rate on unsteady boundary–layer transition is studied with respect to the detectability by means of DIT and the measured transition movement over the pitch cycle. According to the defini-

This work is licensed under the Creative Commons Attribution International License (CC BY). Copyright © 2019 by author(s).

tion of the pitch cycle in Eq. 1 the corresponding pitch rate yields

$$\frac{d\Theta}{dt} = 2\pi f_{\text{rotor}}\hat{\Theta} \cdot sin(2\pi f_{\text{rotor}} t). \quad (5)$$

In this study, the pitch rate was altered by an independent variation of the pitch amplitude $\hat{\Theta}$ and the rotation frequency f_{rotor}. The pitch amplitudes varied between $\hat{\Theta} = 1.6, 2.9$ and $6.2\,\text{deg}$ at constant collective pitch and pitch frequency (test cases i,ii and iii in Tab. 1). The effect of pitch frequency is investigated by changing the rotation rate of the rotor from $f_{\text{rotor}} = 11.8\,\text{Hz}$ to $f_{\text{rotor}} = 23.6\,\text{Hz}$, leaving collective and cyclic pitch unaltered (test cases iii and iv in Tab. 1).

Detectability The DIT signal strength is quantified for each test case by calculating the averaged absolute value of the DIT signal peaks around $\Delta(t/T) = \pm 0.025$ of the maximum and minimum values of the DIT peaks over the pitch cycle (see e.g. Fig. 11, *top*). The peak noise, or scatter, is quantified by the averaged standard deviation of the peak values within the same phase ranges, which were considered to compute the signal strength. The signal strength and the associated scatter are plotted for the test cases used to study the effect of pitch amplitude and pitch frequency in Fig. 12.

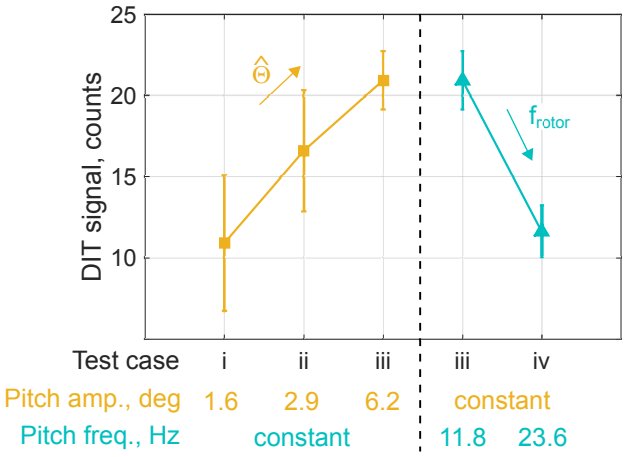


Figure 12: Maximum averaged absolute value of DIT signal peak and associated scatter for test cases i–iv

The maximum signal peak increases and the scatter decreases with increasing pitch amplitude, which consequently favors the detectability of boundary–layer transition by means of DIT. The increased peak-to-noise ratio at higher pitch amplitudes is due to the larger displacement of the boundary–layer transition position between the time instants of the two associated images. This was demonstrated by Wolf et al.[9] who applied the DIT method to steady infrared transition data, which has been obtained at different angles of attack on a two–dimensional DSA–9A airfoil (see Fig. 8 in Ref.[9]). However, Wolf et al.[9] also showed that, if the transition displacement is too large, for instance due to an excessive phase separation between images $\Delta t/T$, the detectability is debased due to the existence of a double peak in the signal.

The results in Fig. 12 for test cases iii and iv indicate that the maximum signal peak decreases as the pitch frequency is increased, whereas the scatter level remains similar. For all cases, the phase separation between DIT image pairs was kept constant at $\Delta t f_{\text{rotor}} = 0.05$. Therefore, the time difference between two images is doubled as the frequency is halved. Hence, at $f_{\text{rotor}} = 11.8\,\text{Hz}$ the model surface has twice the time to react to the different surface temperature between images. The transition shift is the same for both pitch frequencies as it depends on the difference in pitch angles $\Delta\Theta = (d\Theta/dt) \cdot \Delta t$. The change of pitch angles is also unaltered for the both cases because the phase separation $\Delta t f_{\text{rotor}}$ between images is constant, i.e. $\Delta\Theta = 2\pi\Delta t f_{\text{rotor}} \cdot sin(2\pi f_{\text{rotor}} t)$, see Eq. 5.

Transition Positions The measured boundary–layer transition positions for the pitch amplitude study are plotted against the pitch cycle in Fig. 13. For reasons of clarity, the data in Fig. 13 and the following figures have been reduced. All data samples were binned to 50 windows throughout the pitch cycle and each bin was median filtered to smooth out existing scatter. The bars confine the minimum and maximum of the data considered for each bin, respectively. Before binning, obvious invalid outliers were removed, for instance in phase ranges close to the pitch minimum or at streamwise positions in the vicinity of the leading and trailing edges.

In Fig. 13, DIT data is extracted at $r/R = 0.74$, which is in the vicinity of the pressure transducers at $r/R = 0.77$ but outside the turbulent wedge emanating from the sensor cavities. The streamwise range of occuring boundary–layer transition is extended to both directions as the pitch amplitude is increased, leading to an intersection of the scatter plots at $t/T \approx 0.35$ and $t/T \approx 0.81$. These phases are in the vicinity to the phases corresponding to the respective mean pitch angle, i.e $t/T = 0.25$ and $t/T = 0.75$. The same effect was observed by Richter et al.[38] who studied the pitch amplitude effect on unsteady boundary–layer transition on a two–dimensional (2D) EDI-M109 airfoil. They showed that the intersection points correspond to phases with comparable sectional lift coefficient.

To compare with DIT results, the σc_p method[2] was applied. The detected phases corresponding to

This work is licensed under the Creative Commons Attribution International License (CC BY). Copyright © 2019 by author(s).

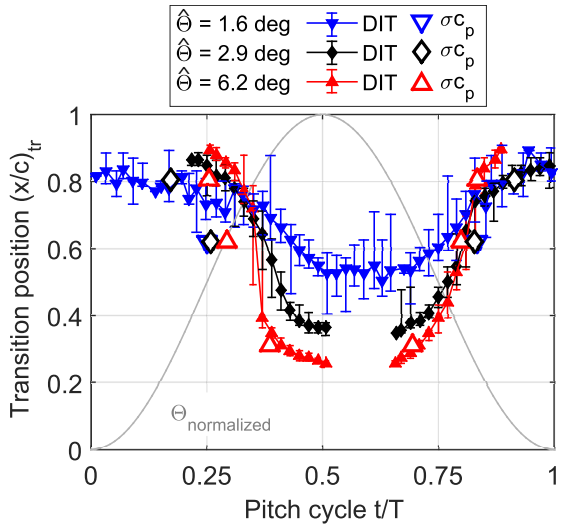


Figure 13: Pitch amplitude effect on transition positions versus pitch cycle for test cases i, ii and iii (see Tab. 1); DIT data extracted at $r/R = 0.74$, σc_p data at $r/R = 0.77$

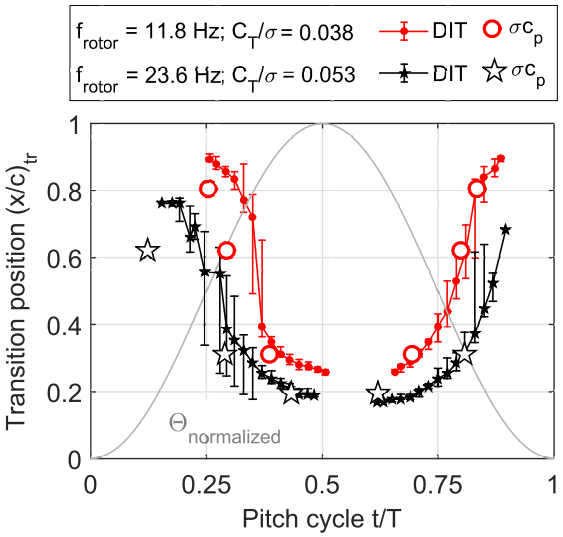


Figure 14: Pitch frequency effect on transition positions versus pitch cycle for test cases iii and iv (see Tab. 1); DIT data extracted at $r/R = 0.79$, σc_p data at $r/R = 0.77$

boundary–layer transition at the respective sensor positions are marked by open symbols in Fig. 13. The σc_p results compare well during downstroke and comprise a maximum difference of $\Delta\,(x/c)_{\mathrm{tr}} \approx 0.25$ during upstroke. The upstream shift compared to the DIT results at $t/T < 0.5$ can be attributed to premature boundary–layer transition at the pressure tap cavities as observed in Fig. 10 (*top*) at $r/R = 0.77$.

The measured transition positions for the pitch frequency study are plotted against the pitch cycle in Fig. 14. The qualitative evolution of the transition positions is similar to the results discussed in Fig. 13. In general, the unsteady transition results are consistently further upstream at the higher pitch frequency of $f_{\mathrm{rotor}} = 23.6\,\mathrm{Hz}$. Since the axial inflow remains unchanged in both cases, the inflow angle to the rotor blades increases at higher rotation rates. The resulting larger effective angle of attack causes a higher blade loading of $C_T/\sigma = 0.053$ at $f_{\mathrm{rotor}} = 23.6\,\mathrm{Hz}$ compared to $C_T/\sigma = 0.038$ at $f_{\mathrm{rotor}} = 11.8\,\mathrm{Hz}$, which, in turn, results in boundary–layer transition positions further upstream. The higher Reynolds number at $f_{\mathrm{rotor}} = 23.6\,\mathrm{Hz}$ also causes boundary–layer transition to occur upstream. Hence, the results in Fig. 14 include the superposed effects of both Reynolds number and blade loading. As for the cases presented in Fig. 13, the σc_p results indicate boundary–layer transition further upstream during upstroke and good agreement to DIT results during downstroke. At $(x/c)_{\mathrm{tr}} = 0.62$ in Fig. 14, only a single peak in the σc_p measuring signal could be identified. It occurs close to the reversal of the transition motion and was attributed to the upstroke motion.

Transition Hysteresis The effects of pitch amplitude and frequency on the transition hysteresis become more apparent in Fig. 15, where the measured transition positions are plotted as function of the instantaneous pitch angle for the test cases presented in Fig. 13 and Fig. 14, respectively.

The results in the Fig. 15 (*top*) indicate that the hysteresis, i.e. the difference in pitch angle at equal transition position, increases with pitch amplitude. The finding confirms the results of the pitch amplitude study by Richter et al.[38] and extends the applicability to rotor conditions. Moreover, a smaller hysteresis is measured using σc_{p} compared to DIT. This holds true for the transition positions of the test cases used in order to study the effect of pitch frequency in Fig. 15 (*bottom*), as well.

Richter et al.[8,37] measured the isolated effect of pitch frequency on the transition hysteresis on a pitching 2D DSA–9A airfoil at $M = 0.30$ and $Re = 1.8 \times 10^6$. They used hot–films[37] and compared the findings to results from DIT and σc_p[8]. Wolf et al.[9] studied the effect of both pitch amplitude and frequency on the transition hysteresis. They used the same 2D DSA–9A airfoil model as Richter et al.[8,37] One of their findings showed that the hystereses obtained by σc_p and DIT scale with the respective pitch rates (see Eq. 5). The hystereses measured in these studies[8,9] are plotted in Fig. 16 (*top*) as functions of the pitch rate with filled symbols representing DIT and open symbols standing for σc_p.

This work is licensed under the Creative Commons Attribution International License (CC BY). Copyright © 2019 by author(s).

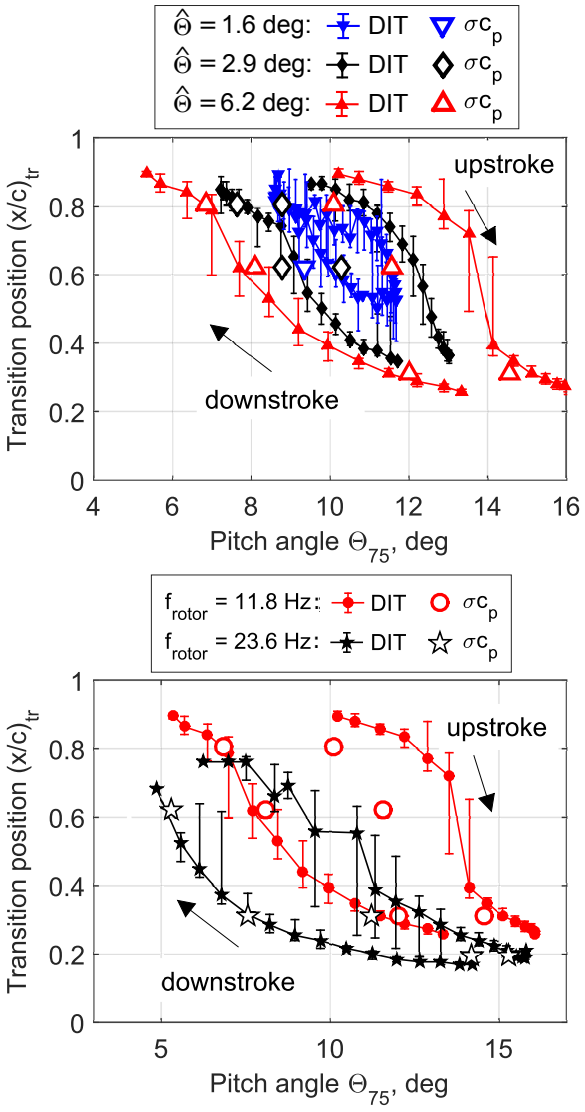


Figure 15: Unsteady transition positions versus pitch angle for different pitch amplitudes (*top*) and different pitch frequencies (*bottom*)

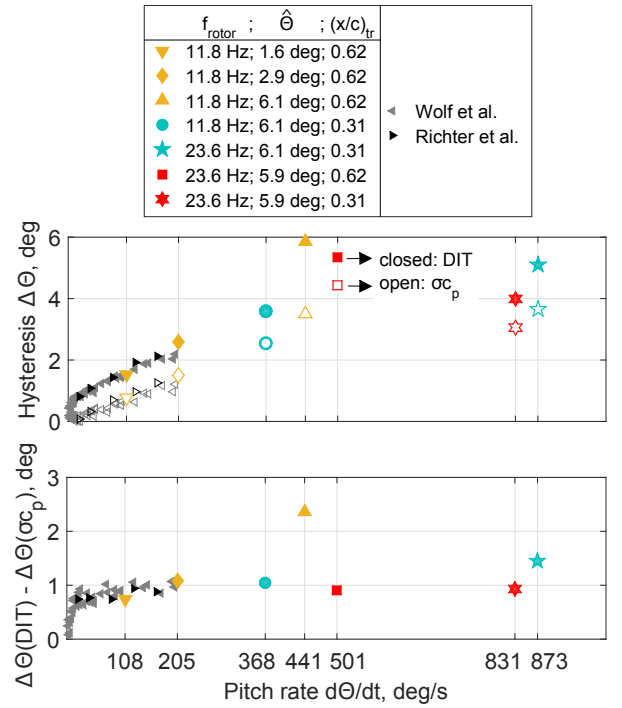


Figure 16: Hysteresis obtained with DIT and σc_p (*top*) and temperature–lag related hysteresis (*bottom*) against pitch rate compared to results from Wolf et al.[9] and Richter et al.[8]

The pitch rate associated with each data point is calculated as the mean value between the two phases when transition passes the streamwise position of the respective pressure transducers. Richter et al.[8] extracted the data at $(x/c)_{\mathrm{tr}} = 0.22$ and at $(x/c)_{\mathrm{tr}} = 0.23$ for DIT and σc_p, respectively. The data from Wolf et al.[9] is acquired at $(x/c)_{\mathrm{tr}} = 0.31$. The graph is complemented by the hystereses measured in this study at $(x/c)_{\mathrm{tr}} = 0.62$ and at $(x/c)_{\mathrm{tr}} = 0.31$. At these streamwise positions, data for both DIT and σc_p could be extracted for the test cases used to study the effect of pitch amplitude (in orange), of pitch frequency (in blue), and for test case v (in red). The observed trends in literature[8,9], i.e. the increasing hysteresis at increasing pitch rates for results obtained by both DIT and σc_p, are confirmed by the data presented in this paper. Additionally, the results from this work extend the range of existing pitch rate data from $d\Theta/dt < 200\ \mathrm{deg/s}$ up to $d\Theta/dt = 873\ \mathrm{deg/s}$, while providing the first transition hysteresis data set obtained by DIT on rotating blades so far.

The hysteresis obtained with DIT includes an additional temperature–lag related hysteresis due to the model surface time response to the changing temperature footprint as result of the boundary–layer transition displacement[8,9,30]. Assuming that the hysteresis values obtained by σc_p display the aerodynamic hysteresis only, the differences between the results from DIT and σc_p $\left[\Delta\Theta(DIT) - \Delta\Theta(\sigma c_p)\right]$, express the temperature–lag related measurement hysteresis of DIT[9]. The measurement hysteresis is plotted as a function of pitch rate in Fig. 16 (*bottom*). The results from Wolf et al.[9] indicate a convergence of $\Delta\Theta(DIT) - \Delta\Theta(\sigma c_p)$ to $\approx 1\ \mathrm{deg}$, which includes the results from Richter et al.[8] The prescribed trend is confirmed by all data points from the present study, except for the outlier at $d\Theta/dt = 441\ \mathrm{deg/s}$. Wolf et al.[9] showed that the measurement hysteresis is minimized when limiting the phase separation between the acquired images for DIT to $\Delta t f < 0.01$, which applies to their data in Fig. 16. The results in this study are acquired at phase differences of $\Delta t f_{\mathrm{rotor}} = 0.05$ and the data points from Richter et al.[8] are obtained at phase

This work is licensed under the Creative Commons Attribution International License (CC BY). Copyright © 2019 by author(s).

differences between $0.006 < \Delta tf < 0.046$ with greater values at higher pitch rates. However, the data in Fig. 16 (*bottom*) at $d\Theta/dt < 205\,\mathrm{deg/s}$ do not indicate any influence by the different phase deltas.

4.2.2. Transition Map

Test case v (see Tab. 1) was selected for further analysis of transition positions across the blade span over the entire pitch cycle. The experimental and numerical results are shown in Fig. 17 (*left*) and (*right*), respectively. Both 'transition maps' comprise the same contour levels and the data is plotted in polar coordinates with the pitch cycle and the corresponding pitch angles in counter–clockwise direction and with the normalized blade radius in radial direction. Overall, the results reveal remarkable agreement.

The experimental data was analyzed at seventeen radial positions between $0.26 \leq r/R \leq 0.97$. For each radius, the detected transition positions were cleared from outliers and valid data was median filtered to 50 bins within the pitch cycle as described above. The resulting contour plot in Fig. 17 (*left*) is derived from the measured boundary–layer transition positions $(x/c)_{\mathrm{tr}}$ as well as from 2D linearly interpolated data at grid points corresponding to the nearest phase position with available data and the seventeen evaluated radial sections. The phase shift of maximal upstream and downstream transition positions due to hysteresis effects with respect to the vertical axis in the plot is clearly distinguishable. The data displayed in the bottom left and top right quadrant of the graph at $0.25 < t/T < 0.5$ and $0.75 < t/T < 1$ reveal the gradual upstream and downstream movement of transition during upstroke and downstroke, respectively. The three–dimensional distribution of $(x/c)_{\mathrm{tr}}$ along the blade span can be deduced by the curved isolines between contour levels. At phase instants between $0.3 < t/T < 0.45$, boundary–layer transition occurs further upstream at more outboard radii, whereas between $0.75 < t/T < 0.87$ transition is shifted downstream at higher radii. In the same phase domains, the measured transition positions reveal a noticeable downstream shift at the most outboard radii of $r/R > 0.85$.

The numerical results in Fig. 17 (*right*) have been corrected by the measured delta between transition onset and the point of 50 % intermittency using the correction function $\Delta_{50\,\%}$ from Fig. 8. The numerical data was extracted at 48 line–in–flight cuts at each time step, which corresponds to $\Delta(t/T) = 1/360$. The two data sets show good quantitative and qualitative agreement, especially with respect to the curvature of contour isolines at $0.25 < t/T < 0.5$ and $0.75 < t/T < 1$. As suggested by the measurement results at $r/R > 0.85$, the numerical results in these phase domains confirm the downstream shift of boundery-layer transition towards the blade tip, as found in the steady test cases in Sec. 4.1. In between $0.3 < t/T < 0.4$, a relative upstream shift of the experimental transition positions can be distinguished in the vicinity of $r/R = 0.5$, which is not visible in the numeric result. In this region, the measurement results were sampled in between the roughness element at $r/R = 0.49$ and the pressure transducer cavities at $r/R = 0.53$, yet the detected positions remain to be influenced by the turbulent wedges at these radii (see Fig. 10, *top*).

The numerically predicted upstream and downstream motion of boundary–layer transition is faster than the measured data suggests. This is indicated by the closer spacing of contour isolines for

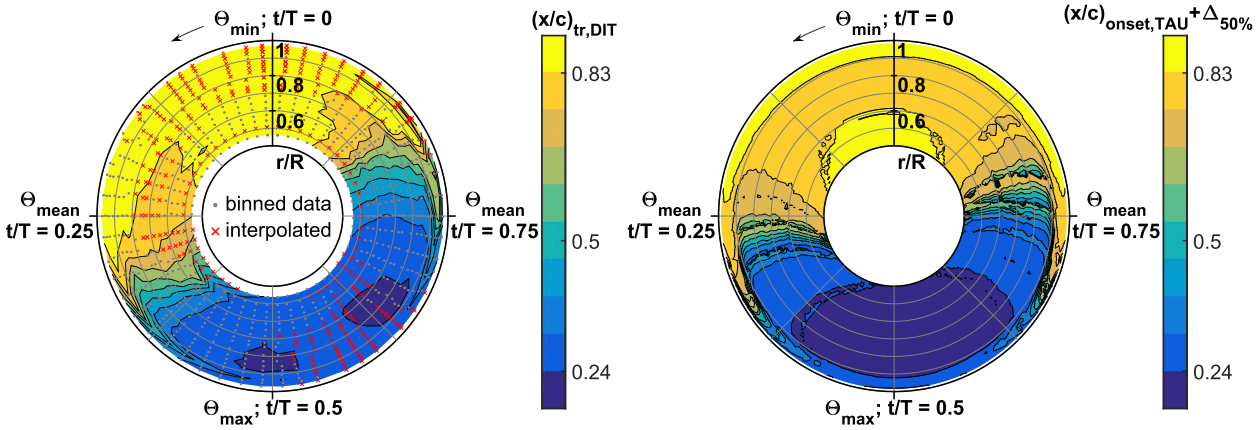


Figure 17: Unsteady boundary–layer transition map at f_{rotor} = 23.6 Hz, $\bar{\Theta}_{75} = 9.0\,\mathrm{deg}$ and $\hat{\Theta} = 5.9\,\mathrm{deg}$ as measured with DIT (*left*) and calculated in TAU (*right*)

This work is licensed under the Creative Commons Attribution International License (CC BY). Copyright © 2019 by author(s).

the numerical solution as compared to the experimental results at the phases during upstroke and downstroke when Θ_{mean} is passed. Moreover, the numerical results during upstroke at $t/T \approx 0.3$ and during downstroke at $t/T \approx 0.8$ indicate a discontinuous transition movement.

The data shown in Fig. 17 are extracted at $r/R = 0.75$ and plotted as function of the pitch angle together with the measured results using the σc_p method in Fig. 18.

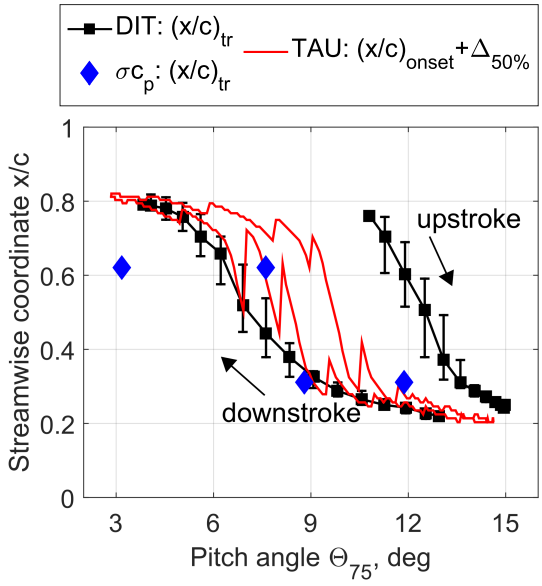


Figure 18: Measured (DIT, σc_p) and calculated (TAU) transition results at $r/R = 0.75$ for test case v

The corrected numerical transition positions and the measured DIT results cover the same streamwise range. The TAU and DIT solutions agree especially during downstroke. The closer spacing of contour level lines observed in Fig. 17 is reflected as larger gradient of the curves for the TAU solution. The above mentioned discontinuities in the numerical results appear as unphysical spikes in Fig. 17, especially at pitch angles with a large transition gradient. There is a noticeable difference of the transition hysteresis between the numerical and experimental results. Although the hysteresis of the numerical solution is hard to quantify due to the existing spikes in the data, it can be distinguished that the hysteresis of the calculated results is smaller than the hystereses of both DIT and σc_p results. Presuming that the hysteresis measured by σc_p yields the true aerodynamic transition hysteresis, the finding here supports the hypothesis from Richter et al.[37] They measured the transition hysteresis with hot–films on a 2D pitching DSA–9A airfoil and showed that it exceeds the maximum pitch angle difference, which is caused by the unsteadiness in lift. The numerical transition prediction applied in this study is based on criteria derived from static airfoil aerodynamics. Therefore, no larger hysteresis than the one caused by the unsteadiness in lift can be expected, and it is plausible that the hysteresis as measured by σc_p is underestimated.

5. CONCLUSION

This work presents the first systematic study of measured unsteady boundary–layer transition on the suction side of a subscale helicopter rotor blade equipped with a DSA–9A airfoil. The analysis of measured results is complemented by a comparison to numerical computations using the semi–empirical AHD criterion to model boundary–layer transition due to Tollmien–Schlichting instabilities. The main findings are summarized as follows:

- Unsteady boundary–layer transition positions have successfully been measured, showing reasonable comparison to measurement results for steady test cases with collective pitch angles only and deviations due to hysteresis effects.
- The detectability of transition positions by DIT, in terms of signal peak–to–noise ratio, increases with increasing pitch amplitude and decreases with increasing pitch frequency at constant phase differences between images.
- The independent variations of pitch amplitude and pitch frequency reveal plausible trends with respect to the measured transition movement and the related hysteresis.
- Transition positions measured using the σc_p method show reasonable agreement to DIT results. Deviations are due to premature boundary–layer transition triggered at the pressure tap cavities and due to the temperature–lag related measurement hysteresis in DIT.
- Hysteresis effects, both aerodynamic and for DIT also temperature–lag related, scale with pitch rate. Previous findings obtained on 2D pitching airfoils are confirmed and extended to rotor conditions for pitch rates of up to $d\Theta/dt = 873\,\mathrm{deg/s}$.
- Transition maps of unsteady experimental and numerical results reveal the three–dimensional distribution of the transition positions along the blade span as function of the pitch cycle. The results obtained by numeric modeling of unsteady boundary–layer transition yield noticeable agreement with experimental results.

This work is licensed under the Creative Commons Attribution International License (CC BY). Copyright © 2019 by author(s).

ACKNOWLEDGMENTS

This work was conducted within the framework of the DLR project FASTrescue. James Heineck's participation was accommodated under the NASA-DLR Memorandum of Understanding Implementing Arrangement for Experimental Optical Methods Applied to Helicopter Research. The authors would like to thank Anthony D. Gardner and Markus Krebs (DLR Göttingen) for their fruitful advise and the assistance during experiments. Moreover, the Gauss Centre for Supercomputing e.V. (www.gauss-centre.eu) is greatfully acknowledged for funding this project by providing computing time using the GCS SuperMUC at the Leibniz Supercomputing Centre (LRZ, www.lrz.de).

REFERENCES

[1] P. F. Lorber and F. O. Carta. Unsteady Transition Measurements on a Pitching Three–Dimensional Wing. In *5th Symposium on Numerical and Physical Aspects of Aerodynamic Flows*, Long Beach, CA, USA, January 13–15 1992.

[2] A. D. Gardner and K. Richter. Boundary layer transition determination for periodic and static flows using phase-averaged pressure data. *Experiments in Fluids*, 56(6):119–131, 2015. doi: 10.1007/s00348-015-1992-9.

[3] M. Raffel, F. De Gregorio, K. de Groot, O. Schneider, W. Sheng, G. Gibertini, and A. Seraudie. On the Generation of a Helicopter Aerodynamic Database. *The Aeronautical Journal*, 115(1164):103–112, 2011. doi: 10.1017/S0001924000005492.

[4] T. Schwermer, A. D. Gardner, and M. Raffel. A Novel Experiment to Understand the Dynamic Stall Phenomenon in Rotor Axial Flight. *Journal of the American Helicopter Society*, 64(1):1–11, 2019. doi: 10.4050/JAHS.64.012004.

[5] A. D. Overmeyer and P. B. Martin. Measured Boundary Layer Transition and Rotor Hover Performance at Model Scale. In *55*th *AIAA Aerospace Sciences Meeting*, Grapevine, TX, USA, January 9–13 2017. doi: 10.2514/6.2017-1872.

[6] A. Weiss, A. D. Gardner, C. Klein, and M. Raffel. Boundary-layer transition measurements on mach-scaled helicopter rotor blades in climb. *CEAS Aeronautical Journal*, 8(4):613–623, 2017. doi: 10.1007/s13272-017-0263-2.

[7] M. Raffel and C. B. Merz. Differential Infrared Thermography for Unsteady Boundary-Layer Transition Measurments. *AIAA Journal*, 52(9): 2090–2093, 2014. doi: 10.2514/1.J053235.

[8] K. Richter, C. C. Wolf, A. D. Gardner, and C. B. Merz. Detection of Unsteady Boundary Layer Transition Using Three Experimental Methods. In *54th AIAA Aerospace Sciences Meeting*, San Diego, CA, USA, January 4–8, 2016. doi: 10.2514/6.2016-1072.

[9] C. C. Wolf, C. Mertens, A. D. Gardner, C. Dollinger, and A. Fischer. Optimization of differential infrared thermography for unsteady boundary layer transition measurement. *Experiments in Fluids*, 60(19):1–13, 2019. doi: 10.1007/s00348-018-2667-0.

[10] A. D. Overmeyer, J. T. Heineck, and C. C. Wolf. Unsteady Boundary Layer Transition Measurements on a Rotor in Forward Flight. In *AHS International 74th Annual Forum & Technology Display*, Phoenix, AZ, USA, May 14–17 2018.

[11] A. D. Gardner, C. C. Wolf, J. T. Heineck, M. Barnett, and M. Raffel. Helicopter rotor boundary layer transition measurement in forward flight using an infrared camera. In *VFS 75th Annual Forum & Technology Display*, Philadelphia, PA, USA, May 13–16 2019.

[12] J. G. Coder. OVERFLOW rotor hover simulations using advanced turbulence and transition modeling. In *55th AIAA Aerospace Sciences Meeting*, Grapevine, TX, USA, January 9–13 2017. doi: 10.2514/6.2017-1432.

[13] B. A. O. Vieira, M. P. Kinzel, and M. D. Maughmer. CFD hover prediction including boundary-layer transition. In *55th AIAA Aerospace Sciences Meeting*, Grapevine, TX, USA, January 9–13 2017. doi: 10.2514/6.2017-1665.

[14] A. Parwani and J. G. Coder. Effect of Laminar–Turbulent Transition Modeling on PSP Rotor Hover Predictions. In *56th AIAA Aerospace Sciences Meeting*, Kissimmee, FL, USA, January 8–12 2018. doi: 10.2514/6.2018-0308.

[15] Q. Zhao, J. Wang, and C. Sheng. Numerical Simulations and Comparisons of PSP and S–76 Rotors in Hover. In *56th AIAA Aerospace Sciences Meeting*, Kissimmee, FL, USA, January 8–12 2018. doi: 10.2514/6.2018-1780.

[16] J. A. Carnes and J. G. Coder. Computational Assessment of Laminar–Turbulent Transition for a Rotor in Forward–Flight conditions. In *VFS 75th Annual Forum & Technology Display*, Philadelphia, PA, USA, May 13–16 2019.

[17] B.-Y. Min, C. A. Reimann, B. Wake, S. K. Jee, and J. D. Baeder. Hovering Rotor Simulation using OVERFLOW with Improved Turbulence Model. In *56th AIAA Aerospace Sciences Meeting*, Kissimmee, FL, USA, January 8–12 2018. doi: 10.2514/6.2018-1779.

[18] C. C. Heister. Semi-/empirical transition prediction and application to an isolated rotor in

This work is licensed under the Creative Commons Attribution International License (CC BY). Copyright © 2019 by author(s).

hover. *International Journal of Engineering Systems Modelling and Simulation*, 4(1-2), 2012. doi: 10.1504/IJESMS.2012.044845.

[19] F. Richez, A. Nazarians, and C. Lienard. Assessment of laminar–turbulent transition modeling methods for the prediction of helicopter rotor performance. In *43rd European Rotorcraft Forum*, Milan, Italy, September 12–15 2017.

[20] C. C. Heister. A method for approximate prediction of laminar–turbulent transition on helicopter rotors. *Journal of the American Helicopter Society*, 63(3):1–14, 2018. doi: 10.4050/JAHS.63.032008.

[21] K. Kaufmann, P. Ströer, F. Richez, C. Lienard, P. Gardarein, N. Krimmelbein, and A. D. Gardner. Validation of boundary-layer-transition computations for a rotor with axial inflow. In *VFS 75th Annual Forum & Technology Display*, Philadelphia, PA, USA, May 13–16 2019.

[22] T. Schwermer, K. Richter, and M. Raffel. Development of a Rotor Test Facility for the Investigation of Dynamic Stall. In A. Dillmann, G. Heller, E. Krämer, C. Wagner, and C. Breitsamter, editors, *New Results in Numerical and Experimental Fluid Mechanics X. Notes on Numerical Fluid Mechanics and Multidisciplinary Design*, volume 132, pages 663–673, Cham, 2016. Springer Int. Publishing. doi: 10.1007/978-3-319-27279-5_58.

[23] A. Vuillet, M. Allongue, J. J. Philippe, and A. Desopper. Performance and Aerodynamic Development of the Super Puma MK II Main Rotor with New SPP 8 blade tip design. In *15th European Rotorcraft Forum*, Amsterdam, Holland, September 12–15 1989.

[24] M. Raffel and J. T. Heineck. Mirror-Based Image Derotation for Aerodynamic Rotor Measurements. *AIAA Journal*, 52(6):1337–1341, 2014. doi: 10.2514/1.J052836.

[25] D. Schwamborn, T. Gerhold, and R. Heinrich. The DLR TAU-Code: Recent Applications in Research and Industry. *AIAA Journal*, 32(8):2066–2072, 1994. doi: 10.2514/3.12149.

[26] F. R. Menter. Two-equation eddy-viscosity transport turbulence model for engineering applications. *AIAA Journal*, 32(8):2066–2072, 1994. doi: 10.2514/3.12149.

[27] D. Arnal, M. Habiballah, and E. Coustols. Laminar instability theory and transition criteria in two and three-dimensional flow. *La Recherche Aérospatiale (English Edition)*, 2:45–63, 1984.

[28] P. R. Spalart and C. L. Rumsey. Effective inflow conditions for turbulence models in aerodynamic calculations. *AIAA Journal*, 45(10):2544–2553, 2007. doi: 10.2514/1.29373.

[29] A. Weiss, A. D. Gardner, T. Schwermer, C. Klein, and M. Raffel. On the effect of rotational forces on rotor blade boundary-layer transition. *AIAA Journal*, 57(1):252–266, 2018. doi: 10.2514/1.J057036.

[30] A. D. Gardner, C. Eder, C. C. Wolf, and M. Raffel. Analysis of differential infrared thermography for boundary layer transition detection. *Experiments in Fluids*, 58(9):122–135, 2017. doi: 10.1007/s00348-017-2405-z.

[31] C. Klein, R. H. Engler, U. Henne, and W. E. Sachs. Application of pressure-sensitive paint for determination of the pressure field and calculation of the forces and moments of models in a wind tunnel. *Experiments in Fluids*, 39(2):475–483, 2005. doi: 10.1007/s00348-005-1010-8.

[32] P. R. Ashill, C. J. Betts, and I. M. Gaudet. A wind tunnel study of transition flows on a swept panel wing at high subsonic speeds. In *CEAS 2nd European Forum on Laminar Flow Technology*, Bordeaux, France, June 10–12 1996.

[33] J. H. Stanfield and C. J. Betts. Transition detection technique in use in the DRA Bedford wind tunnels. In *Proceedings of the 7th International Symposium on Flow Visualization*, pages 929–934, Seattle, WA, USA, September 11-14 1995.

[34] H.-P. Kreplin and G. Höhler. Application of the surface hot film technique for laminar flow investigations. In *First European Forum on Laminar Flow Technology*, Hamburg, Germany, May, 16-18 1992.

[35] G. J. Walker and J. P. Gostelow. Effects of adverse pressure gradients on the nature and length of boundary layer transition. *Journal of Turbomachinery*, 112(2):196–205, 1990. doi: 10.1115/1.2927633.

[36] H. Schlichting and K. Gersten. *Boundary-Layer Theory*. Springer-Verlag Berlin Heidelberg, 9th edition, 2017. doi: 10.1007/978-3-662-52919-5.

[37] K. Richter, S. Koch, A. Goerttler, B. Lütke, C. C. Wolf, and A. Benkel. Unsteady Boundary Layer Transition on the DSA-9A Rotor Blade Airfoil. In *41st European Rotorcraft Forum*, Munich, Germany, September 1–4 2015.

[38] K. Richter, S. Koch, A. D. Gardner, H. Mai, A. Klein, and C. H. Rohardt. Experimental Investigation of Unsteady Transition on a Pitching Rotor Blade Airfoil. *Journal of the American Helicopter Society*, 59(1):1–12, 2014. doi: 10.4050/JAHS.59.012001.

This work is licensed under the Creative Commons Attribution International License (CC BY). Copyright © 2019 by author(s).